



1 **Holocene climates of the Iberian Peninsula: pollen-based reconstructions of changes in**  
2 **the west-east gradient of temperature and moisture**

3 Mengmeng Liu<sup>1,\*</sup>, Yicheng Shen<sup>2</sup>, Penelope González-Sampérez<sup>3</sup>, Graciela Gil-Romera<sup>3</sup>,  
4 Cajo J. F. ter Braak<sup>4</sup>, Iain Colin Prentice<sup>1</sup>, Sandy P. Harrison<sup>2</sup>

5 1: Department of Life Sciences, Imperial College London, Silwood Park Campus, Buckhurst  
6 Road, Ascot SL5 7PY, UK

7 2: Geography & Environmental Science, Reading University, Whiteknights, Reading, RG6  
8 6AH, UK

9 3: Instituto Pirenaico de Ecología-CSIC, Avda. Montañana 1005, 50059, Zaragoza, Spain

10 4: Biometris (Applied Mathematics and Applied Statistics Centre), Wageningen University &  
11 Research, 6708 PB Wageningen, The Netherlands

12 \*: Corresponding author: Mengmeng Liu (m.liu18@imperial.ac.uk)

13 **Abstract**

14 The Iberian Peninsula is characterised by a steep west-east moisture gradient today, reflecting  
15 the dominance of maritime influences along the Atlantic coast and more Mediterranean-type  
16 climate further east. Holocene pollen records from the Peninsula suggest that this gradient  
17 was less steep during the early to mid-Holocene, possibly reflecting the impact of orbital  
18 changes on circulation and thus regional patterns in climate. Here we use 7121 pollen  
19 samples from 117 sites covering part or all of the last 12,000 years to reconstruct changes in  
20 seasonal temperature and in moisture across the Iberian Peninsula quantitatively. We show  
21 that there is an increasing trend in winter temperature at a regional scale, consistent with  
22 known changes in winter insolation. However, summer temperatures do not show the  
23 decreasing trend through the Holocene that would be expected if they were a direct response  
24 to insolation forcing. We show that summer temperature is strongly correlated with plant-  
25 available moisture ( $\alpha$ ), as measured by the ratio of actual evapotranspiration to equilibrium  
26 evapotranspiration, which declines through the Holocene. The reconstructions also confirm  
27 that the west-east gradient in moisture was considerably less steep than today during the early  
28 to mid-Holocene, indicating that atmospheric circulation changes (possibly driven by orbital  
29 changes) have been important determinants of the Holocene climate of the region.



31 **1. Introduction**

32 The Iberian Peninsula is characterised by a steep west-east gradient in temperature and  
33 moisture today, reflecting the dominance of maritime influences along the Atlantic coast and  
34 more Mediterranean-type climate further east. Projections of future climate change suggest that  
35 the region will become both warmer and drier, but nevertheless show that this west-east  
36 differentiation is maintained. The changes in temperature are projected to be larger and the  
37 occurrence of extreme temperature episodes more frequent in the south-central and eastern  
38 parts of Iberia than in Atlantic coastal areas (Carvalho et al., 2021). Similar gradients are seen  
39 in future projections of precipitation change, with largest reductions in precipitation in the  
40 south-central region (Andrade et al., 2021). However, the stability of these west-east gradients  
41 during the Holocene has been questioned. In particular, the west-east gradient in moisture  
42 appears to have been less pronounced during the middle Holocene (8-4 ka) when cooler  
43 summers and wetter conditions in the Atlantic zone (e.g. Martínez-Cortizas et al., 2009; Mauri  
44 et al., 2015) coincided with the maximum development of mesophytic vegetation further east  
45 and south (Aranbarri et al., 2014, 2015; Carrión et al., 2010, 2009; González-Sampéris et al.,  
46 2017).

47 However, much of the evidence for Holocene climates is based on qualitative interpretations  
48 of vegetation changes, generally interpreted as reflecting changes in moisture availability  
49 (Morellón et al., 2018). Although these records are extensive, they seem to indicate fairly  
50 complex spatial patterns of change. Iberia was included in the quantitative pollen-based  
51 reconstructions of European climate through the Holocene (Mauri et al., 2015). However, most  
52 of the ca 50 sites from Iberia were from the Pyrenees and the inferred patterns across the  
53 Peninsular are therefore largely extrapolated. Furthermore, quantitative reconstructions of  
54 summer temperature made at individual sites using chironomid data (Muñoz Sobrino et al.,  
55 2013; Tarrats et al., 2018) are not consistent with reconstructed changes based on pollen for  
56 the same sites.

57 Here we re-examine the trends in summer and winter temperature and plant-available moisture  
58 through the Holocene across Iberia, using a new and relatively comprehensive compilation of  
59 pollen data (Shen et al., 2021) with age models based on the latest radiocarbon calibration  
60 curve (IntCal20: Reimer et al., 2020). We analyse how these trends are related to external  
61 forcing and quantify whether there are significant differences in west-east gradients through  
62 time.



## 63 2. Methods

64 We used a modified version of Tolerance-weighted Weighted Averaging Partial Least-Square  
65 with a sampling frequency correction (fxTWA-PLS: Liu et al., 2020) to reconstruct three  
66 climate variables: mean temperature of the coldest month (MTCO), mean temperature of the  
67 warmest month (MTWA) and plant-available moisture represented by  $\alpha$ , an estimate of the  
68 ratio of actual evapotranspiration to equilibrium evapotranspiration. The individual and joint  
69 effects of MTCO, MTWA and  $\alpha$  were tested explicitly using canonical correspondence analysis  
70 (CCA). fxTWA-PLS is a modification of the Weighted Average Partial Least-Square (WA-  
71 PLS) approach. The modification produces less compression of reconstructions towards the  
72 centre of the climatic range sampled by the training dataset, by accounting for the climatic  
73 tolerances of individual pollen taxa and the frequency of the sampled climate variable (fx) in  
74 the training dataset (Liu et al., 2020). The fx correction is applied as a weight with the form of  
75  $1/\text{fx}^2$  in the regression (step 7 in Table 1 in Liu et al., 2020). Here (see Appendix A) we make  
76 a further modification of fxTWA-PLS by (a) applying the fx correction separately in both the  
77 taxon calculation and the regression (step 2 and 7 in Table 1 in Liu et al., 2020) as a weight  
78 with the form of  $1/\text{fx}$  and (b) applying P-splines smoothing (Eilers and Marx, 2021) in order to  
79 reduce the dependence of the fx estimation on bin width. The modified version further reduces  
80 the biases at the extremes of the sampled climate range.

81 The modern pollen training dataset was derived from the SPECIAL Modern Pollen Data Set  
82 (SMPDS: Harrison, 2019). The SMPDS consists of relative abundance records of the 247 most  
83 important pollen taxa from 6458 terrestrial sites from Europe, the Middle East and northern  
84 Eurasia (SI Figure S1). For our analysis, we use the 195 taxa that occur at more than 10 sites.  
85 Modern climate data at each of the sites in the training data set were obtained from Harrison  
86 (2019). The fossil pollen data from the Iberian Peninsula were compiled by Shen et al. (2021)  
87 and obtained from <http://dx.doi.org/10.17864/1947.294>. The taxonomy used by Shen et al.  
88 (2021) is consistent with that employed in the SMPDS. Shen et al. (2021) provides consistent  
89 age models for all the records based on the IntCal20 calibration curve (Reimer et al., 2020) and  
90 the BACON Bayesian age-modelling tool (Blaauw et al., 2021; Blaauw and Christeny, 2011)  
91 using the supervised modelling approach implemented in the `ageR` package (Villegas-Diaz et  
92 al, 2021). We excluded individual pollen samples with large age uncertainties (standard error  
93 larger than 100 years). We also excluded a few samples where the reconstructed values of  $\alpha$   
94 exceed the natural limit of 0 and 1.26. As a result, the climate analyses are based on a fossil  
95 data set of 7121 pollen samples from 117 sites covering part or all of the last 12,000 years



96 (Figure 1).

97 In addition to examining the reconstructions for individual sites, we constructed composite  
98 curves for the Iberian Peninsula as a whole. These curves were constructed after binning the  
99 site-based reconstructions using  $\pm 500$ -year bins. We did 1000 bootstrap resampling of the  
100 reconstructed climate values in each  $\pm 500$ -year bin to avoid the influence of a single value or  
101 a single site on the mean climate value in this bin, and use the standard deviation of the 1000  
102 values to represent the uncertainty of the mean climate value. We constructed linear regression  
103 plots to examine the longitudinal and elevational patterns in the reconstructed climate  
104 variables, and assessed the significance of differences in these trends through time compared  
105 to 0.5 ka based on  $p$  values, with the customary threshold of 0.05.

106 The individual and joint effects of MTCO, MTWA and  $\alpha$  were tested explicitly using canonical  
107 correspondence analysis (CCA).

### 108 3. Results

109 The modified version of fxTWA-PLS reproduces the modern climate reasonably well (Table  
110 1). The performance is best for MTCO ( $R^2$  0.75, RMSEP 4.70, slope 0.91) but is also good for  
111  $\alpha$  ( $R^2$  0.68, RMSEP 0.16, slope 0.78) and MTWA ( $R^2$  0.57, RMSEP 3.47, slope 0.71). The  
112 correlations between pollen records and each of the three bioclimate variables, as assessed by  
113 CCA, were strong for both modern climate data and fossil reconstructions (Table 2). The  
114 variance inflation factor scores are all less than 6, so there are no multicollinearity problems  
115 (Table 2). Furthermore, the taxa that contribute most strongly to reconstructing colder/warmer  
116 or wetter/drier climates show predictable patterns consistent with their known ecological  
117 preferences (SI Table S2).

118 Winters were generally colder than present during the early to mid-Holocene, as shown by the  
119 coherent patterns of reconstructed anomalies at individual sites (Fig. 2a, 2d). The composite  
120 curve also shows a general increase in winter temperatures through time (Fig. 3a), consistent  
121 with the trend in winter insolation (Fig. 3d). The composite curve shows that it was ca 4°C  
122 cooler than today at 11.5 ka and conditions remained cooler than present until ca 2.5 ka. Winter  
123 temperature anomalies show no spatial differentiation between western and eastern Iberia  
124 (Table 3, SI Fig. S2). The similarity of the changes compared to present geographically is  
125 consistent with the idea that the changes in winter temperature are driven by changes in winter  
126 insolation.



127 Summers were somewhat hotter than present in the west and cooler than present in the east  
128 during the early and middle Holocene, as shown by the reconstructed anomalies at individual  
129 sites (Fig. 2b, 2e). This west-east difference could not arise if the changes in summer  
130 temperatures were a direct reflection of the insolation forcing (Fig. 3e). Indeed, the composite  
131 curve shows relatively little change in MTWA (Fig. 3b), confirming that there is no direct  
132 relationship to insolation forcing (Fig. 3e).

133 There is a strong west-east gradient in  $\alpha$  at the present day (Fig. 1), with wetter conditions in  
134 the west and drier conditions in the east. However, the reconstructed anomalies at individual  
135 sites (Fig. 2c, 2f) suggest that west was drier and the east was wetter than present in the mid-  
136 Holocene, resulting in a flatter west-east gradient. The west-east gradient is significantly  
137 different from present between 9.5 ~ 3.5 ka (Fig. 4, Table 3), implying stronger moisture  
138 advection into the continental interior during the mid-Holocene. The change in gradient is seen  
139 in both high and low elevation sites (SI Fig. S3). There is also significant change in  $\alpha$  with  
140 elevation between 9.5 ~ 4.5 ka (Table 3, SI Fig. S4).

141 Summer temperatures are strongly correlated with changes in  $\alpha$ , both in the modern data set at  
142 a European scale and in the fossil data set from Iberia (Fig. 5). The patterns of reconstructed  
143 anomalies in MTWA and  $\alpha$  at individual sites are also coherent (Fig. 2b, 2c, 2e, 2f), showing  
144 drier conditions and hotter summers than present in the west and wetter conditions with cooler  
145 summers in the east during the early to mid-Holocene. The west-east gradient in MTWA was  
146 significantly different from present between 9.5 and 3.5 ka (Table 3, SI Fig. S5), the interval  
147 when the gradient in  $\alpha$  was also significantly different from present. Again, the change in the  
148 east-west gradient is registered at both high and low elevation sites (SI Fig. S6). However,  
149 there is no significant change in MTWA with elevation except 7.5 ka (Table 3, SI Fig. S7).

#### 150 **4. Discussion**

151 We have shown that there was a gradual increase in MTCO over the Holocene, both for most  
152 of the individual sites represented in the data set and for Iberia as a whole. Colder winters in  
153 southern Europe during the mid-Holocene (6 ka) are a feature of many earlier reconstructions  
154 (e.g. Cheddadi et al., 1997; Wu et al., 2007). A general warming trend over the Holocene is  
155 seen in gridded reconstructions of winter season (December, January, February) temperatures  
156 as reconstructed using the modern analogue approach by Mauri et al. (2015), although there is  
157 somewhat less millennial-scale variability in these reconstructions (SI Fig. S8). Nevertheless,



158 their reconstructions show a cooling of 3°C in the early Holocene are comparable in magnitude  
159 to the ca 4°C cooling at 11.5 ka reconstructed here. Although they show conditions slightly  
160 cooler than present persisting up to 1 ka, the differences are very small (ca 0.5°C) after 2 ka,  
161 again consistent with our reconstructions of MTCO similar to present by 2.5 ka. Quantitative  
162 reconstructions of winter temperature are available for 5 terrestrial sites from the Iberian  
163 Peninsula in the Kaufman et al. (2020) compilation of Holocene climate information. These  
164 sites all show a general trend of winter warming over the Holocene, but the magnitude of the  
165 change at some of the individual sites is much larger (ca 10°C) and there is no assessment of  
166 the uncertainty on these reconstructions. The composite curve of Kaufman et al. (2020) shows  
167 an increasing trend in MTCO through the Holocene but with large uncertainties (SI Fig. S8).  
168 Our reconstructed trend in winter temperature is consistent with the changes in insolation  
169 forcing at this latitude during the Holocene, and is also consistent with transient climate model  
170 simulations of the winter temperature response to changing insolation forcing over the late  
171 Holocene in this region (SI Fig. S9). Thus, we suggest that changes in winter temperatures are  
172 a direct consequence of insolation forcing.

173 We have shown that there is no overall trend in MTWA during the Holocene. According to our  
174 reconstructions, summer temperatures fluctuated between ca 0.5°C above or below modern  
175 temperature. The lack of coherent trend in MTWA is consistent with the gridded  
176 reconstructions of summer (June, July, August) temperature in the Mauri et al. (2015) data set  
177 and also with the 5 terrestrial sites from Iberia included in the Kaufman et al. (2020) data set.  
178 However, the patterns shown in the three data sets are very different from one another. Mauri  
179 et al. (2015) suggest the early Holocene was colder than today, and although temperatures  
180 similar to today were reached at 9 ka, most of the Holocene was characterised by cooler  
181 summers. Kaufman et al. (2020), however, showed warmer than present conditions during the  
182 early Holocene although they also show cooler conditions during the later Holocene. The  
183 differences between the three data sets probably reflect differences in the number of records  
184 used, but the lack of coherency points to there not being a strong, regionally coherent signal of  
185 summer temperature changes during the Holocene.

186 The chironomid record from Laguna de la Roya covers the late glacial and terminates at 10.5  
187 ka (Muñoz Sobrino et al., 2013). The reconstructed July temperature during the early Holocene  
188 is ca 12–13 °C, which is considerably cooler than today at this site. However, the authors  
189 caution that these samples have poor analogues and the record should be interpreted with



190 caution. Chironomid-based reconstructions of July temperature at Basa de la Mora (Tarrats et  
191 al., 2018), a high elevation site in the Pyrenees, indicate temperatures within  $\pm 0.5^\circ \text{C}$  of the  
192 modern during the early to mid-Holocene (10–6 ka), similar to our regional composite  
193 reconstructions. However, they show a persistent cooling of  $1.5^\circ \text{C}$  compared to present  
194 between 4.5 and 2 ka, not seen in these reconstructions. Furthermore, direct comparison of our  
195 reconstructions of MTWA at Basa de la Mora (SI Fig. S10) to the chironomid-based  
196 reconstructions highlights that the two records show very different trajectories, since the  
197 pollen-based reconstruction of this site shows a consistent warming trend throughout the  
198 Holocene. Although Tarrats et al. (2018) argue that discrepancies between their temperature  
199 reconstructions and pollen-based reconstructions reflects the fact that the vegetation of Iberia,  
200 including the mountain areas, is largely driven by moisture changes and perhaps is not a good  
201 indicator of temperature, we have shown that there is sufficient information in the pollen  
202 records to reconstruct temperature and moisture independently (Table 2, Table S2). Thus, the  
203 cause of the differences between the pollen-based and chironomid-based reconstructions at  
204 Basa de la Mora is presumably related to methodology. In particular, the chironomid  
205 reconstructions use a training data set that does not include samples from the Pyrenees, or  
206 indeed the Mediterranean more generally, and may therefore not provide good analogues for  
207 Holocene changes at this site.

208 The lack of a clear trend in MTWA in our reconstructions is not consistent with insolation  
209 forcing, which shows a declining trend during the Holocene nor is it consistent with simulated  
210 changes in MTWA in transient climate model simulations of the summer temperature response  
211 to changing insolation forcing over the late Holocene in this region (SI Fig. S9). The change in  
212 moisture gradient during the mid-Holocene, however, suggests an alternative explanation  
213 whereby changes in summer temperature are a response to land-surface feedbacks associated  
214 with changes in moisture. Specifically, the increased advection of moisture into eastern Iberia  
215 created wetter conditions leading to increased evapotranspiration, less allocation of available  
216 net radiation to sensible heating, and resulting in cooler air temperatures. Our reconstructions  
217 show that the west-east moisture gradient in mid-Holocene was significantly flatter than the  
218 steep moisture gradient today, implying a significant increase in moisture advection into the  
219 continental interior during this period. Mauri et al. (2015) also showed that summers were  
220 generally wetter than present in the east but drier than present in the west at early to mid-  
221 Holocene, supporting the idea of a flatter west-east gradient. Stronger moisture advection is  
222 not a feature of the transient climate model simulations, which may explain why these



223 simulations do not show a strong modification of the insolation-driven changes in summer  
224 temperature. The failure of the current generation of climate models to simulate the observed  
225 strengthening of moisture transport into Europe and Eurasia during the mid-Holocene has been  
226 noted by other studies (e.g. Bartlein et al., 2017; Mauri et al., 2014). This data-model mismatch  
227 highlights the need for better modelling of land-surface feedbacks on atmospheric circulation  
228 and moisture.

229 Speleothem oxygen-isotope data from the Iberian Peninsula provide support for our pollen-  
230 based reconstructions of changes in the west-east gradient of moisture through the Holocene.  
231 The speleothem records show a progressive increase in temperature from the Younger Dryas  
232 onwards, although the trend is less marked in the west than the east (Baldini et al., 2019). This  
233 warming trend is consistent with our reconstructions of changes in MTCO through the  
234 Holocene. However, speleothem records show distinctly different patterns in moisture  
235 availability, with sites in western Iberia indicating wetter environments during early Holocene  
236 and a transition to drier conditions from ca 7.5 cal ka BP to the present (Stoll et al., 2013;  
237 Thatcher et al., 2020) while eastern sites record wetter conditions persisting from 9 to 4 cal ka  
238 (Walczak et al., 2015). This finding would support the weaker west to east moisture gradient  
239 shown by our results.

240 Pollen data are widely used for the quantitative reconstruction of past climates (see discussion  
241 in Bartlein et al., 2011). Nevertheless, climate is not the only driver of vegetation changes. On  
242 glacial-interglacial timescales, changes in CO<sub>2</sub> have a direct impact on plant physiological  
243 processes and reductions in plant water-use efficiency at low CO<sub>2</sub> result in vegetation  
244 appearing to reflect drier conditions that were experienced in reality (Farquhar, 1997; Gerhart  
245 and Ward, 2010; Prentice et al., 2017; Prentice and Harrison, 2009). We have not accounted  
246 for the impact of changing CO<sub>2</sub> in our reconstructions of  $\alpha$ , although there are techniques to do  
247 this (Prentice et al., 2011, 2017; Wei et al., 2021). However, the change in CO<sub>2</sub> over the  
248 Holocene was only 40 ppm. Prentice et al. (2021) shows that this change relative to modern  
249 levels has only a small impact on pollen-based reconstructed moisture indices. Furthermore,  
250 accounting for the effect of this change in CO<sub>2</sub> would not affect the reconstructed west-east  
251 gradient through time. A more serious issue for our reconstructions may be the extent to which  
252 the vegetation cover of Iberia was substantially modified by human activities during the  
253 Holocene. While there is no doubt that anthropogenic activities were important at the local  
254 scale and particularly in the later Holocene (e.g. Abel-Schaad and López-Sáez, 2013; Connor





255 et al., 2019; Fyfe et al., 2019; Mighall et al., 2006; Revelles et al., 2015), most of the sites used  
256 for our reconstructions are not associated with archaeological evidence of agriculture or  
257 substantial landscape modification. Furthermore, the consistency of the reconstructed changes  
258 in climate across sites provides support for these being largely a reflection of regional climate  
259 changes.

260 We have used a modified version of fxTWA-PLS to reconstruct Holocene climates of the  
261 Iberian Peninsula because this modification reduced the compression bias in MTCO and  
262 MTWA, and specifically reduces the maximum bias in MTCO, MTWA and  $\alpha$ . Although this  
263 modified approach produces better overall reconstructions (Appendix A), its use does not  
264 change the reconstructed trends in these variables through time (SI Fig. S11). Thus, the finding  
265 that winter temperatures are a direct reflection of insolation forcing whereas summer  
266 temperatures are influenced by land-surface feedbacks and changes in atmospheric circulation  
267 is robust to the method used. However, while we use a much larger data set than previous  
268 reconstructions, the distribution of pollen sites is uneven and the northern part of the Peninsula  
269 is better sampled than the southwest, which could lead to some uncertainties in the  
270 interpretation of changes in the west-east gradient of moisture. It would, therefore, be useful to  
271 specifically target the southwestern part of the Iberian Peninsula for new data collection.  
272 Alternatively, it would be useful to apply the approach used here to the whole of Eurasia, given  
273 that the failure of state-of-the-art climate models to advect moisture into the continental interior  
274 appears to be a feature of the whole region (Bartlein et al., 2017) and not the Peninsula alone.

275

#### 276 **Data and Code Availability**

277 All the data used are public access and cited here. The code used to generate the climate  
278 reconstructions is available at <https://github.com/ml4418/Iberia-paper.git>.

279 **Supplement.** The supplement related to this article is available online.

280 **Competing interests.** We declare that we have no conflict of interest.

281 **Author Contributions.** ML, ICP and SPH designed the study. ML, ICP and CJFtB designed  
282 the modifications to fxTWA-PLS. PG-S and GG-R provided pollen data and insights into the  
283 regional palaeoclimate histories. ML carried out the analyses. ML and SPH wrote the first  
284 draft of the paper and all authors contributed to the final draft.



285 **Acknowledgements.** ML acknowledges support from Imperial College through the Lee  
286 Family Scholarship. YS and SPH acknowledge support from the ERC-funded project GC 2.0  
287 (Global Change 2.0: Unlocking the past for a clearer future; grant number 694481). ICP  
288 acknowledges support from the ERC under the European Union Horizon 2020 research and  
289 innovation programme (grant agreement no: 787203 REALM). This work is a contribution to  
290 the project "Origen y Cuantificación de los Cambios Paleoambientales en el Pirineo:  
291 Variabilidad climatic e impacto humano" (PYCACHU: PID2019-106050RB-I00)" funded by  
292 the Ministerio de Ciencia e Innovación.

293 **Financial support.** This research has been supported by Lee Family Scholarship fund, and  
294 the European Research Council (grant no. GC2.0, 694481, and grant no. REALM, 787203).



295 **References**

- 296 Abel-Schaad, D., López-Sáez, J.A.: Vegetation changes in relation to fire history and human  
297 activities at the Peña Negra mire (Bejar Range, Iberian Central Mountain System, Spain)  
298 during the past 4,000 years. *Veg. Hist. Archaeobot.* 22, 199–214.  
299 <https://doi.org/10.1007/s00334-012-0368-9>, 2013.
- 300 Abel-Schaad, D. and López-Sáez, J. A.: Vegetation changes in relation to fire history and  
301 human activities at the Peña Negra mire (Bejar Range, Iberian Central Mountain System,  
302 Spain) during the past 4,000 years, *Veg. Hist. Archaeobot.*, 22, 199–214,  
303 [doi:10.1007/s00334-012-0368-9](https://doi.org/10.1007/s00334-012-0368-9), 2013.
- 304 Andrade, C., Contente, J. and Santos, J. A.: Climate change projections of dry and wet events  
305 in Iberia based on the WASP-Index, *Climate*, 9(6), [doi:10.3390/cli9060094](https://doi.org/10.3390/cli9060094), 2021.
- 306 Aranbarri, J., Gonzalez Samperiz, P., Valero-Garcés, B., Moreno, A., Gil-Romera, G.,  
307 Sevilla-Callejo, M., Garcia-Prieto, E., Di Rita, F., Mata, M. del Pi., Morellón, M., Magri, D.,  
308 Rodriguez-Lazaro, J. and Carrión, J.: Rapid climatic changes and resilient vegetation during  
309 the Lateglacial and Holocene in a continental region of south-western Europe, *Glob. Planet.*  
310 *Change*, 114, 50–65, [doi:10.1016/j.gloplacha.2014.01.003](https://doi.org/10.1016/j.gloplacha.2014.01.003), 2014.
- 311 Aranbarri, J., González-Sampériz, P., Iriarte, E., Moreno, A., Rojo-Guerra, M., Peña-  
312 Chocarro, L., Valero-Garcés, B., Leunda, M., García-Prieto, E., Sevilla-Callejo, M., Gil-  
313 Romera, G., Magri, D. and Rodríguez-Lázaro, J.: Human–landscape interactions in the  
314 Conquezueta–Ambrona Valley (Soria, continental Iberia): From the early Neolithic land use  
315 to the origin of the current oak woodland, *Palaeogeogr. Palaeoclimatol. Palaeoecol.*, 436, 41–  
316 57, [doi:https://doi.org/10.1016/j.palaeo.2015.06.030](https://doi.org/10.1016/j.palaeo.2015.06.030), 2015.
- 317 Baldini, L. M., Baldini, J. U. L., McDermott, F., Arias, P., Cueto, M., Fairchild, I. J.,  
318 Hoffmann, D. L., Matthey, D. P., Müller, W., Nita, D. C., Ontañón, R., García-Moncó, C. and  
319 Richards, D. A.: North Iberian temperature and rainfall seasonality over the Younger Dryas  
320 and Holocene, *Quat. Sci. Rev.*, 226, 105998,  
321 [doi:https://doi.org/10.1016/j.quascirev.2019.105998](https://doi.org/10.1016/j.quascirev.2019.105998), 2019.
- 322 Bartlein, P. J., Harrison, S. P., Brewer, S., Connor, S., Davis, B. A. S., Gajewski, K., Guiot,  
323 J., Harrison-Prentice, T. I., Henderson, A., Peyron, O., Prentice, I. C., Scholze, M., Seppä, H.,  
324 Shuman, B., Sugita, S., Thompson, R. S., Viau, A. E., Williams, J. and Wu, H.: Pollen-based  
325 continental climate reconstructions at 6 and 21 ka: A global synthesis, *Clim. Dyn.*, 37(3),  
326 775–802, [doi:10.1007/s00382-010-0904-1](https://doi.org/10.1007/s00382-010-0904-1), 2011.
- 327 Bartlein, P. J., Harrison, S. P. and Izumi, K.: Underlying causes of Eurasian midcontinental  
328 aridity in simulations of mid-Holocene climate, *Geophys. Res. Lett.*, 44(17), 9020–9028,  
329 [doi:10.1002/2017GL074476](https://doi.org/10.1002/2017GL074476), 2017.
- 330 Blaauw, M. and Christeny, J. A.: Flexible paleoclimate age-depth models using an  
331 autoregressive gamma process, *Bayesian Anal.*, 6(3), 457–474, [doi:10.1214/11-BA618](https://doi.org/10.1214/11-BA618), 2011.



- 332 Blaauw, M., Christen, J. A., Lopez, M. A. A. V., V., J. E. O. M. G., Belding, T., Theiler, J.,  
333 Gough, B. and Karney, C.: rbacon: Age-depth modelling using Bayesian statistics, [online]  
334 Available from: <https://cran.r-project.org/package=rbacon>, 2021.
- 335 Carrión, J. S., Fernández, S., González-Sampériz, P., Gil-Romera, G., Badal, E., Carrión-  
336 Marco, Y., López-Merino, L., López-Sáez, J. A., Fierro, E. and Burjachs, F.: Expected trends  
337 and surprises in the Lateglacial and Holocene vegetation history of the Iberian Peninsula and  
338 Balearic Islands, *Rev. Palaeobot. Palynol.*, 162(3), 458–475,  
339 doi:<https://doi.org/10.1016/j.revpalbo.2009.12.007>, 2010.
- 340 Carrión, Y., Kaal, J., López-Sáez, J. A., López-Merino, L. and Martínez Cortizas, A.:  
341 Holocene vegetation changes in NW Iberia revealed by anthracological and palynological  
342 records from a colluvial soil, *The Holocene*, 20(1), 53–66, doi:10.1177/0959683609348849,  
343 2009.
- 344 Carvalho, D., Pereira, S. and Rocha, A.: Future surface temperature changes for the Iberian  
345 Peninsula according to EURO-CORDEX climate projections, *Clim. Dyn.*, 56, 1–16,  
346 doi:10.1007/s00382-020-05472-3, 2021.
- 347 Cheddadi, R., Yu, G., Joel, G., Harrison, S., Prentice, I. and Colin, I.: The climate of Europe  
348 6000 years ago, cd, 13, 1, doi:10.1007/s003820050148, 1997.
- 349 Connor, S., Vannière, B., Colombaroli, D., Anderson, R., Carrión, J., Ejarque, A., Gil-  
350 Romera, G., Gonzalez Samperiz, P., Höfer, D., Morales-Molino, C., Revelles, J., Schneider,  
351 H., Knaap, W., Leeuwen, J. and Woodbridge, J.: Humans take control of fire-driven diversity  
352 changes in Mediterranean Iberia's vegetation during the mid-late Holocene, *The Holocene*,  
353 29, 095968361982665, doi:10.1177/0959683619826652, 2019.
- 354 Eilers, P. H. and Marx, B. D.: Practical smoothing: The Joys of P-splines, edited by P. H.  
355 Eilers and B. D. Marx, Cambridge University Press., 2021.
- 356 Farquhar, G. D.: Carbon dioxide and vegetation, *Science (80- )*, 278(5342), 1411,  
357 doi:10.1126/science.278.5342.1411, 1997.
- 358 Fyfe, R. M., Woodbridge, J., Palmisano, A., Bevan, A., Shennan, S., Burjachs, F., Legarra  
359 Herrero, B., García Puchol, O., Carrión, J. S., Revelles, J. and Roberts, C. N.: Prehistoric  
360 palaeodemographics and regional land cover change in eastern Iberia, *Holocene*, 29(5), 799–  
361 815, doi:10.1177/0959683619826643, 2019.
- 362 Gerhart, L. M. and Ward, J. K.: Plant responses to low [CO<sub>2</sub>] of the past, *New Phytol.*,  
363 188(3), 674–695, doi:<https://doi.org/10.1111/j.1469-8137.2010.03441.x>, 2010.
- 364 González-Sampériz, P., Aranbarri, J., Pérez-Sanz, A., Gil-Romera, G., Moreno, A., Leunda,  
365 M., Sevilla-Callejo, M., Corella, J. P., Morellón, M., Oliva, B. and Valero-Garcés, B.:  
366 Environmental and climate change in the southern Central Pyrenees since the Last Glacial  
367 Maximum: A view from the lake records, *Catena*, 149, 668–688,  
368 doi:<https://doi.org/10.1016/j.catena.2016.07.041>, 2017.



- 369 Granados, I. and Toro, M.: Recent warming in a high mountain lake (Laguna Cibera, Central  
370 Spain) inferred by means of fossil chironomids, *J. Limnol.*, 59 (suppl., 109–119,  
371 doi:10.4081/jlimnol.2000.s1.109, 2000.
- 372 Harrison, S. P.: Modern pollen data for climate reconstructions, version 1 (SMPDS), ,  
373 doi:http://dx.doi.org/10.17864/1947.194, 2019.
- 374 Kaufman, D., McKay, N., Routson, C., Erb, M., Davis, B., Heiri, O., Jaccard, S., Tierney, J.,  
375 Dätwyler, C., Axford, Y., Brussel, T., Cartapanis, O., Chase, B., Dawson, A., de Vernal, A.,  
376 Engels, S., Jonkers, L., Marsicek, J., Moffa-Sánchez, P., Morrill, C., Orsi, A., Rehfeld, K.,  
377 Saunders, K., Sommer, P. S., Thomas, E., Tonello, M., Tóth, M., Vachula, R., Andreev, A.,  
378 Bertrand, S., Biskaborn, B., Bringué, M., Brooks, S., Caniupán, M., Chevalier, M., Cwynar,  
379 L., Emile-Geay, J., Fegyveresi, J., Feurdean, A., Finsinger, W., Fortin, M.-C., Foster, L., Fox,  
380 M., Gajewski, K., Grosjean, M., Hausmann, S., Heinrichs, M., Holmes, N., Ilyashuk, B.,  
381 Ilyashuk, E., Juggins, S., Khider, D., Koinig, K., Langdon, P., Larocque-Tobler, I., Li, J.,  
382 Lotter, A., Luoto, T., Mackay, A., Magyari, E., Malevich, S., Mark, B., Massafiero, J.,  
383 Montade, V., Nazarova, L., Novenko, E., Pařil, P., Pearson, E., Peros, M., Pienitz, R.,  
384 Płóciennik, M., Porinchu, D., Potito, A., Rees, A., Reinemann, S., Roberts, S., Rolland, N.,  
385 Salonen, S., Self, A., Seppä, H., Shala, S., St-Jacques, J.-M., Stenni, B., Syrykh, L., Tarrats,  
386 P., Taylor, K., van den Bos, V., Velle, G., Wahl, E., Walker, I., Wilmshurst, J., Zhang, E. and  
387 Zhilich, S.: A global database of Holocene paleotemperature records, *Sci. Data*, 7(1), 115,  
388 doi:10.1038/s41597-020-0445-3, 2020.
- 389 Liu, M., Prentice, I. C., ter Braak, C. J. F. and Harrison, S. P.: An improved statistical  
390 approach for reconstructing past climates from biotic assemblages, *Proc. R. Soc. A Math.*,  
391 476(2243), doi:https://doi.org/10.1098/rspa.2020.0346, 2020.
- 392 Martínez-Cortizas, A., Costa-Casais, M. and López-Sáez, J. A.: Environmental change in  
393 NW Iberia between 7000 and 500cal BC, *Quat. Int.*, 200(1), 77–89,  
394 doi:https://doi.org/10.1016/j.quaint.2008.07.012, 2009.
- 395 Mauri, A., Davis, B. A. S., Collins, P. M. and Kaplan, J. O.: The influence of atmospheric  
396 circulation on the mid-Holocene climate of Europe: a data–model comparison, *Clim. Past*,  
397 10(5), 1925–1938, doi:10.5194/cp-10-1925-2014, 2014.
- 398 Mauri, A., Davis, B. A. S., Collins, P. M. and Kaplan, J. O.: The climate of Europe during the  
399 Holocene: A gridded pollen-based reconstruction and its multi-proxy evaluation, *Quat. Sci.*  
400 *Rev.*, 112, 109–127, doi:10.1016/j.quascirev.2015.01.013, 2015.
- 401 Mighall, T. M., Martínez Cortizas, A., Biester, H. and Turner, S. E.: Proxy climate and  
402 vegetation changes during the last five millennia in NW Iberia: Pollen and non-pollen  
403 palynomorph data from two ombrotrophic peat bogs in the North Western Iberian Peninsula,  
404 *Rev. Palaeobot. Palynol.*, 141(1–2), 203–223, doi:10.1016/j.revpalbo.2006.03.013, 2006.
- 405 Millet, L., Rius, D., Galop, D., Heiri, O. and Brooks, S. J.: Chironomid-based reconstruction  
406 of Lateglacial summer temperatures from the Ech palaeolake record (French western  
407 Pyrenees), *Palaeogeogr. Palaeoclimatol. Palaeoecol.*, 315–316, 86–99,  
408 doi:https://doi.org/10.1016/j.palaeo.2011.11.014, 2012.



- 409 Morellón, M., Aranbarri, J., Moreno, A., González-Sampérez, P. and Valero-Garcés, B. L.:  
410 Early Holocene humidity patterns in the Iberian Peninsula reconstructed from lake, pollen  
411 and speleothem records, *Quat. Sci. Rev.*, 181, 1–18,  
412 doi:<https://doi.org/10.1016/j.quascirev.2017.11.016>, 2018.
- 413 Muñoz Sobrino, C., Heiri, O., Hazekamp, M., van der Velden, D., Kirilova, E. P., García-  
414 Moreiras, I. and Lotter, A. F.: New data on the Lateglacial period of SW Europe: a high  
415 resolution multiproxy record from Laguna de la Roya (NW Iberia), *Quat. Sci. Rev.*, 80, 58–  
416 77, doi:<https://doi.org/10.1016/j.quascirev.2013.08.016>, 2013.
- 417 Prentice, I. C. and Harrison, S. P.: Ecosystem effects of CO<sub>2</sub> concentration: evidence from  
418 past climates, *Clim. Past*, 5(3), 297–307, doi:10.5194/cp-5-297-2009, 2009.
- 419 Prentice, I. C., Meng, T., Wang, H., Harrison, S. P., Ni, J. and Wang, G.: Evidence of a  
420 universal scaling relationship for leaf CO<sub>2</sub> drawdown along an aridity gradient, *New Phytol.*,  
421 190(1), 169–180, doi:<https://doi.org/10.1111/j.1469-8137.2010.03579.x>, 2011.
- 422 Prentice, I. C., Cleator, S. F., Huang, Y. H., Harrison, S. P. and Roulstone, I.: Reconstructing  
423 ice-age palaeoclimates: Quantifying low-CO<sub>2</sub> effects on plants, *Glob. Planet. Change*, 149,  
424 166–176, doi:<https://doi.org/10.1016/j.gloplacha.2016.12.012>, 2017.
- 425 Prentice, I. C., Villegas-Diaz, R. and Harrison, S. P.: Accounting for atmospheric carbon  
426 dioxide variations in pollen-based reconstruction of past hydroclimates, *Glob. Planet.*  
427 *Change*, 2021.
- 428 Reimer, P. J., Austin, W. E. N., Bard, E., Bayliss, A., Blackwell, P. G., Bronk Ramsey, C.,  
429 Butzin, M., Cheng, H., Edwards, R. L., Friedrich, M., Grootes, P. M., Guilderson, T. P.,  
430 Hajdas, I., Heaton, T. J., Hogg, A. G., Hughen, K. A., Kromer, B., Manning, S. W.,  
431 Muscheler, R., Palmer, J. G., Pearson, C., Van Der Plicht, J., Reimer, R. W., Richards, D. A.,  
432 Scott, E. M., Southon, J. R., Turney, C. S. M., Wacker, L., Adolphi, F., Büntgen, U., Capano,  
433 M., Fahrni, S. M., Fogtmann-Schulz, A., Friedrich, R., Köhler, P., Kudsk, S., Miyake, F.,  
434 Olsen, J., Reinig, F., Sakamoto, M., Sookdeo, A. and Talamo, S.: The IntCal20 Northern  
435 Hemisphere radiocarbon age calibration curve (0–55 cal kBP), *Radiocarbon*, 62(4), 725–757,  
436 doi:10.1017/RDC.2020.41, 2020.
- 437 Revelles, J., Cho, S., Iriarte, E., Burjachs, F., van Geel, B., Palomo, A., Piqué, R., Peña-  
438 Chocarro, L. and Terradas, X.: Mid-Holocene vegetation history and Neolithic land-use in  
439 the Lake Banyoles area (Girona, Spain), *Palaeogeogr. Palaeoclimatol. Palaeoecol.*, 435, 70–  
440 85, doi:10.1016/j.palaeo.2015.06.002, 2015.
- 441 Shen, Y., Sweeney, L., Liu, M., Lopez Saez, J. A., Pérez-Díaz, S., Luelmo-Lautenschlaeger,  
442 R., Gil-Romera, G., Hoefler, D., Jiménez-Moreno, G., Schneider, H., Prentice, I. C. and  
443 Harrison, S. P.: Reconstructing burnt area during the Holocene: an Iberian case study, *Clim.*  
444 *Past Discuss.*, 2021, 1–23, doi:10.5194/cp-2021-36, 2021.
- 445 Stoll, H. M., Moreno, A., Mendez-Vicente, A., Gonzalez-Lemos, S., Jimenez-Sanchez, M.,  
446 Dominguez-Cuesta, M. J., Edwards, R. L., Cheng, H. and Wang, X.: Paleoclimate and



- 447 growth rates of speleothems in the northwestern Iberian Peninsula over the last two glacial  
448 cycles, *Quat. Res.*, 80, 284–290, doi:10.1016/j.yqres.2013.05.002, 2013.
- 449 Tarrats, P., Heiri, O., Valero-Garcés, B., Cañedo-Argüelles, M., Prat, N., Rieradevall, M. and  
450 González-Sampéris, P.: Chironomid-inferred Holocene temperature reconstruction in Basa de  
451 la Mora Lake (Central Pyrenees), *The Holocene*, 28(11), 1685–1696,  
452 doi:10.1177/0959683618788662, 2018.
- 453 Thatcher, D. L., Wanamaker, A. D., Denniston, R. F., Asmerom, Y., Polyak, V. J., Fullick,  
454 D., Ummenhofer, C. C., Gillikin, D. P. and Haws, J. A.: Hydroclimate variability from  
455 western Iberia (Portugal) during the Holocene: Insights from a composite stalagmite isotope  
456 record, *The Holocene*, 30(7), 966–981, doi:https://doi.org/10.1177/0959683620908648,  
457 2020.
- 458 Villegas-Díaz, Roberto; Cruz-Silva, Esmeralda; Harrison, S. P.: ageR: Supervised age  
459 models, , doi:10.5281/zenodo.4636715, 2021.
- 460 Walczak, I. W., Baldini, J. U. L., Baldini, L. M., McDermott, F., Marsden, S., Standish, C.  
461 D., Richards, D. A., Andreo, B. and Slater, J.: Reconstructing high-resolution climate using  
462 CT scanning of unsectioned stalagmites: A case study identifying the mid-Holocene onset of  
463 the Mediterranean climate in southern Iberia, *Quat. Sci. Rev.*, 127, 117–128,  
464 doi:https://doi.org/10.1016/j.quascirev.2015.06.013, 2015.
- 465 Wei, D., González-Sampéris, P., Gil-Romera, G., Harrison, S. P. and Prentice, I. C.: Seasonal  
466 temperature and moisture changes in interior semi-arid Spain from the last interglacial to the  
467 Late Holocene, *Quat. Res.*, 101, 143–155, doi:DOI: 10.1017/qua.2020.108, 2021.
- 468 Wu, H., Guiot, J., Brewer, S. and Guo, Z.: Climatic changes in Eurasia and Africa at the last  
469 glacial maximum and mid-Holocene: reconstruction from pollen data using inverse  
470 vegetation modelling, *Clim. Dyn.*, 29(2), 211–229, doi:10.1007/s00382-007-0231-3, 2007.
- 471



472 **Figure and Table Captions**

473 Figure 1. Map showing the location of the 117 fossil sites in the Iberian Peninsula used for  
474 climate reconstructions. Sites lower than 1000 m above sea level are shown as squares, sites  
475 higher than 1000 m above sea level are shown as triangles. The base maps show modern (a)  
476 mean temperature of the coldest month (MTCO), (b) mean temperature of the warmest month  
477 (MTWA), and (c) plant-available moisture as represented by  $\alpha$ , an estimate of the ratio of  
478 actual evapotranspiration to equilibrium evapotranspiration.

479 Figure 2. Reconstructed anomalies in climate at individual sites through time. The sites are  
480 grouped into high (>1000m) and low (<1000m) elevation sites and organised from west to east.  
481 Grey cells indicate periods or longitudes with no data. The individual plots show the anomalies  
482 in reconstructed (a,d) mean temperature of the coldest month (MTCO), (b,e) mean temperature  
483 of the warmest month (MTWA), and (c,f) plant-available moisture as represented by  $\alpha$ , an  
484 estimate of the ratio of actual evapotranspiration to equilibrium evapotranspiration. The  
485 anomalies are expressed as deviations of the mean value in each bin ( $\pm 500$  years) from the  
486 value at 0.5 ka at each site.

487 Figure 3. Reconstructed composite changes (anomalies to 0.5 ka) in (a) mean temperature of  
488 the coldest month (MTCO), (b) mean temperature of the warmest month (MTWA) and (c)  
489 plant-available moisture as represented by  $\alpha$ , through the Holocene compared to changes in  
490 (d) winter and (e) summer insolation for the latitude of the Iberian Peninsula, using  $\pm 500$   
491 years as the bin. The black lines show mean values across sites, with vertical line segments  
492 showing the standard deviations of mean values using 1000 bootstrap cycles of site  
493 resampling.

494 Figure 4. Changes in the west-east gradient of plant-available moisture as represented by  
495 anomalies in  $\alpha$  relative to 0.5 ka at individual sites through the Holocene. The red lines show  
496 the regression lines. The shades indicate the 95 % confidence intervals of the regression lines

497 Figure 5. The relationship between mean temperature of the warmest month (MTWA) and  
498 plant-available moisture as represented by  $\alpha$  (a) in the modern climate data set, and (b) in the  
499 Holocene reconstructions.

500 Table 1. Leave-out cross-validation (with geographically and climatically close sites  
501 removed) fitness of the modified version of fxTWA-PLS, for mean temperature of the coldest  
502 month (MTCO), mean temperature of the warmest month (MTWA) and plant-available  
503 moisture ( $\alpha$ ), with p-spline smoothed fx estimation, using bins of 0.02, 0.02 and 0.002,  
504 showing results for all the components. RMSEP is the root-mean-square error of prediction.  
505  $\Delta$ RMSEP is the per cent change of RMSEP using the current number of components than  
506 using one component less. p assesses whether using the current number of components is



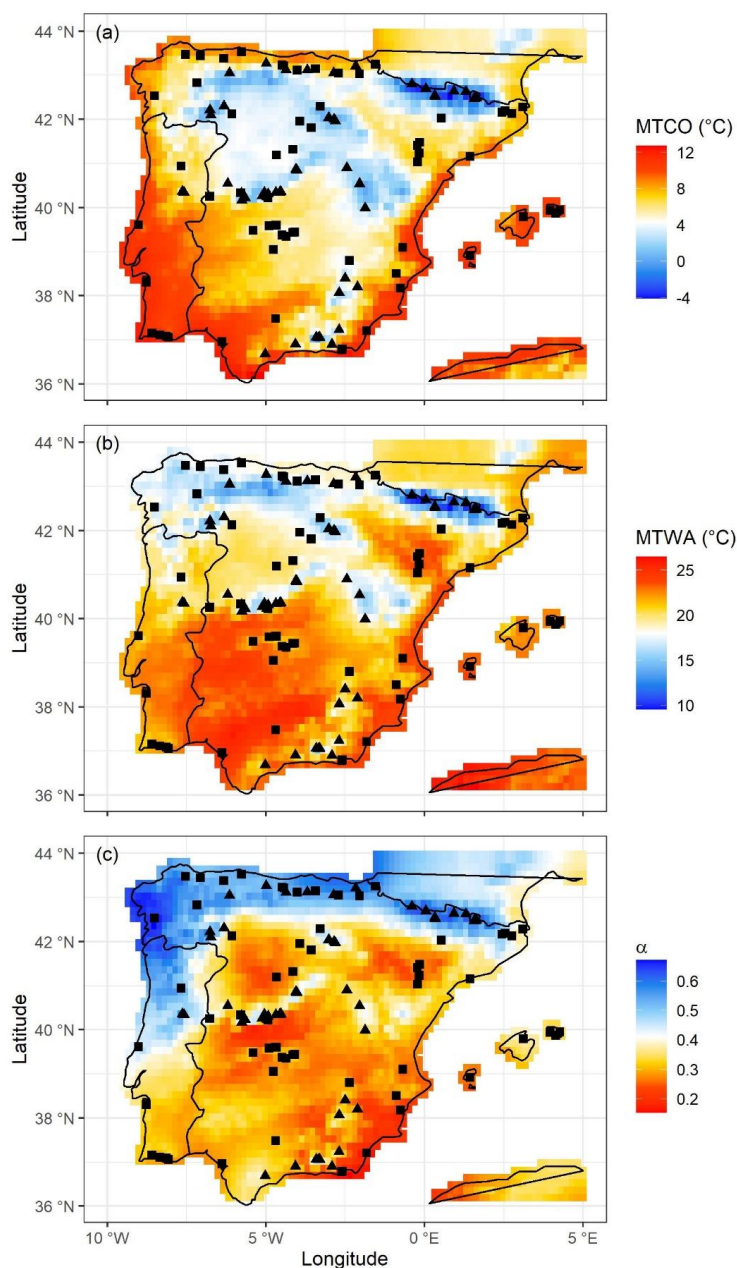


507 significantly different from using one component less, which is used to choose the last  
508 significant number of components (indicated in bold) to avoid over-fitting. The degree of  
509 overall compression is assessed by linear regression of the cross-validated reconstructions  
510 onto the climate variable,  $b_1$ ,  $b_1.se$  are the slope and the standard error of the slope,  
511 respectively. The closer the slope ( $b_1$ ) is to 1, the less the overall compression is.

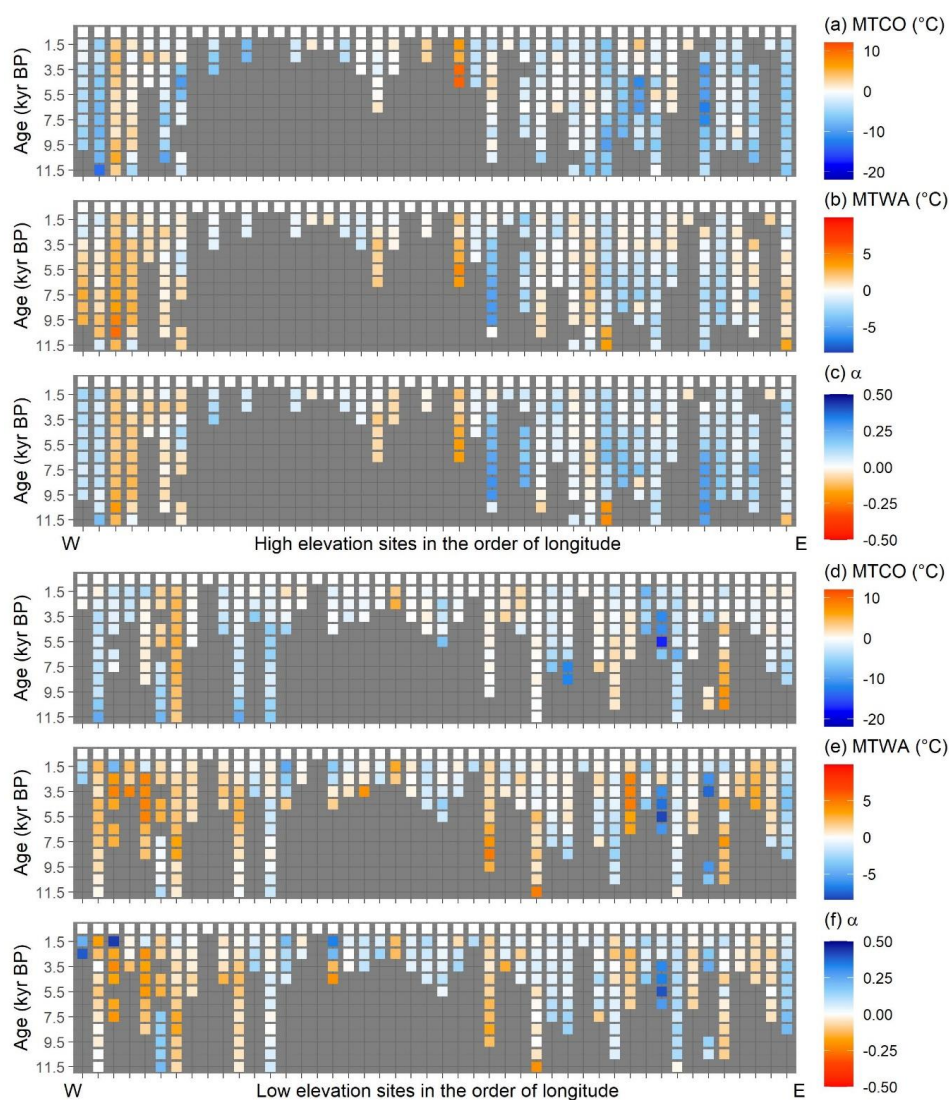
512 Table 2. Canonical Correspondence Analysis (CCA) result of modern and fossil-  
513 reconstructed MTCO, MTWA and  $\alpha$ . The summary statistics for the ANOVA-like  
514 permutation test (999 permutations) are also shown. VIF is the variance inflation factor, Df is  
515 the number of degrees of freedom,  $\chi^2$  is the constrained eigenvalue (or the sum of  
516 constrained eigenvalues for the whole model), F is significance, and Pr (>F) is the  
517 probability.

518 Table 3. Assessment of the significance of anomalies to 0.5 ka through time with latitude and  
519 elevation. The slope is obtained by linear regression of the anomaly onto the longitude or  
520 elevation.  $p$  is the significance of the slope (bold parts:  $p < 0.05$ ).  $x_0$  is the point where the  
521 anomaly is 0 in the linear equation, which indicates longitude or elevation where the anomaly  
522 changes sign.

523 Figure 1. Map showing the location of the 117 fossil sites in the Iberian Peninsula used for  
524 climate reconstructions. Sites lower than 1000 m above sea level are shown as squares, sites  
525 higher than 1000 m above sea level are shown as triangles. The base maps show modern (a)  
526 mean temperature of the coldest month (MTCO), (b) mean temperature of the warmest month  
527 (MTWA), and (c) plant-available moisture as represented by  $\alpha$ , an estimate of the ratio of  
528 actual evapotranspiration to equilibrium evapotranspiration.  
529

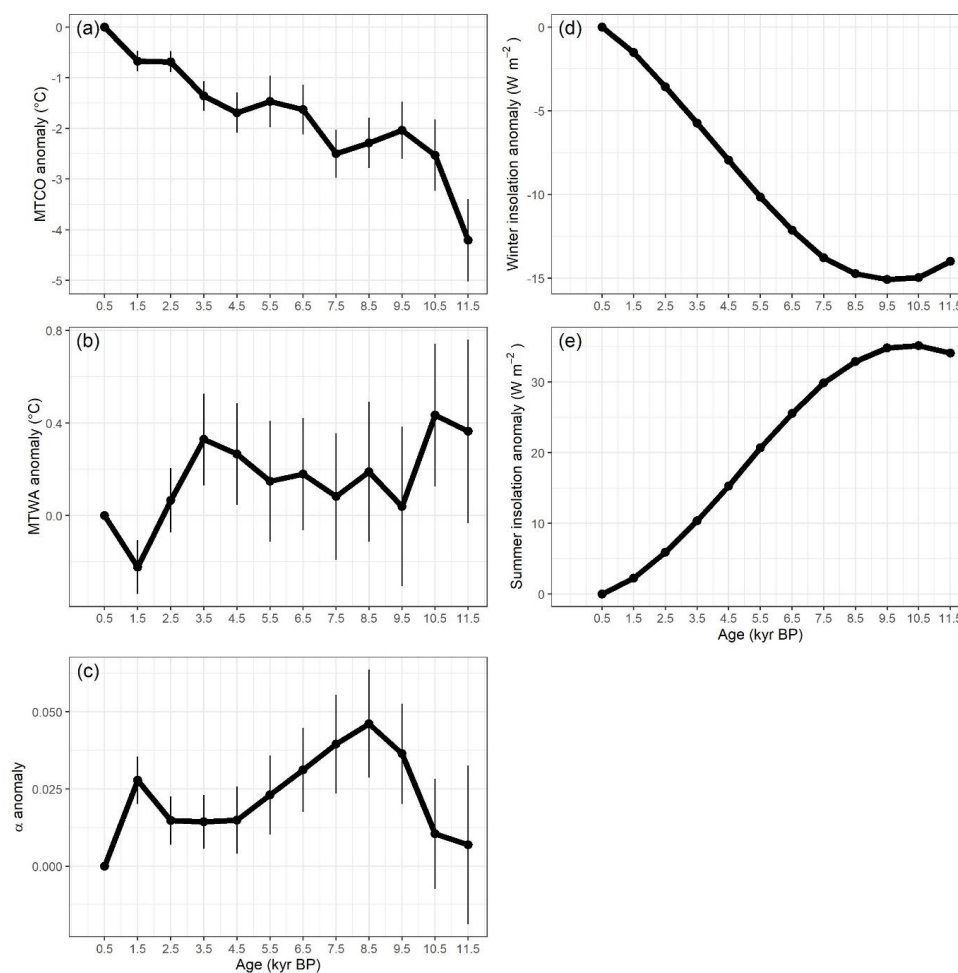


531 Figure 2. Reconstructed anomalies in climate at individual sites through time. The sites are  
532 grouped into high (>1000m) and low (<1000m) elevation sites and organised from west to  
533 east. Grey cells indicate periods or longitudes with no data. The individual plots show the  
534 anomalies in reconstructed (a,d) mean temperature of the coldest month (MTCO), (b,e) mean  
535 temperature of the warmest month (MTWA), and (c,f) plant-available moisture as  
536 represented by  $\alpha$ , an estimate of the ratio of actual evapotranspiration to equilibrium  
537 evapotranspiration. The anomalies are expressed as deviations of the mean value in each bin  
538 ( $\pm 500$  years) from the value at 0.5 ka at each site.  
539



540

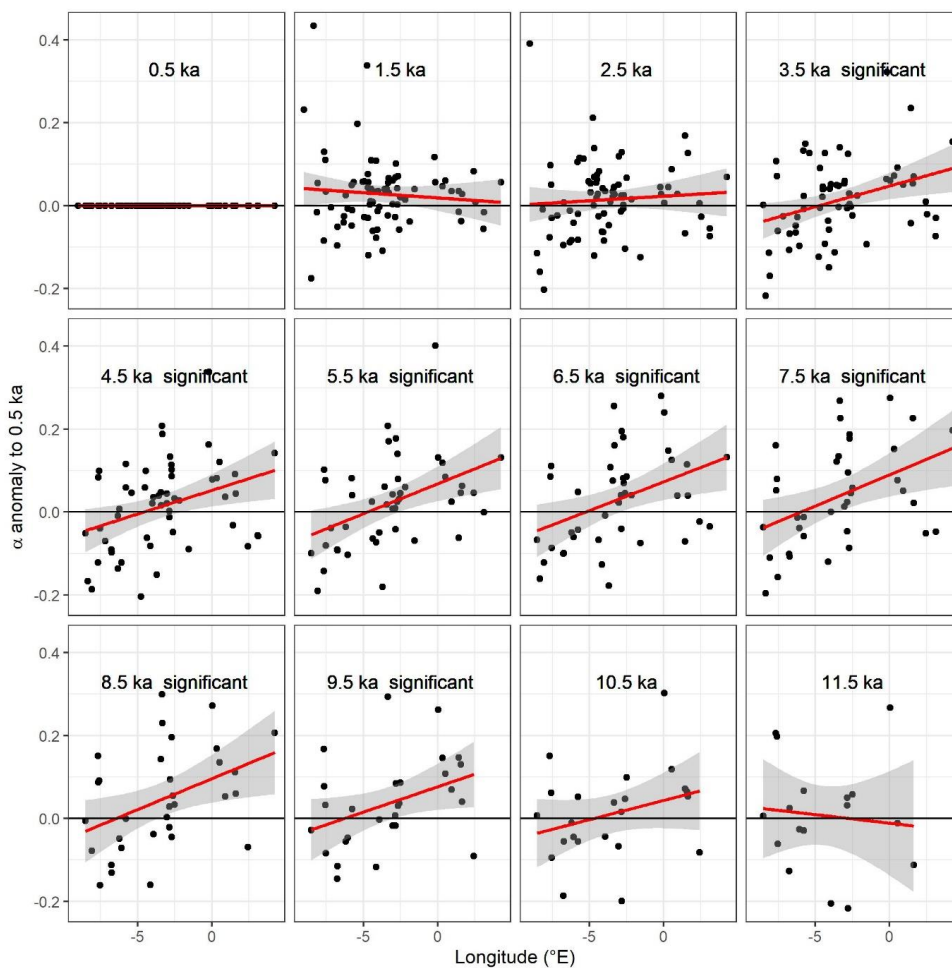
541 Figure 3. Reconstructed composite changes (anomalies to 0.5 ka) in (a) mean temperature of  
542 the coldest month (MTCO), (b) mean temperature of the warmest month (MTWA) and (c)  
543 plant-available moisture as represented by  $\alpha$ , through the Holocene compared to changes in  
544 (d) winter and (e) summer insolation for the latitude of the Iberian Peninsula, using  $\pm 500$   
545 years as the bin. The black lines show mean values across sites, with vertical line segments  
546 showing the standard deviations of mean values using 1000 bootstrap cycles of site  
547 resampling.  
548



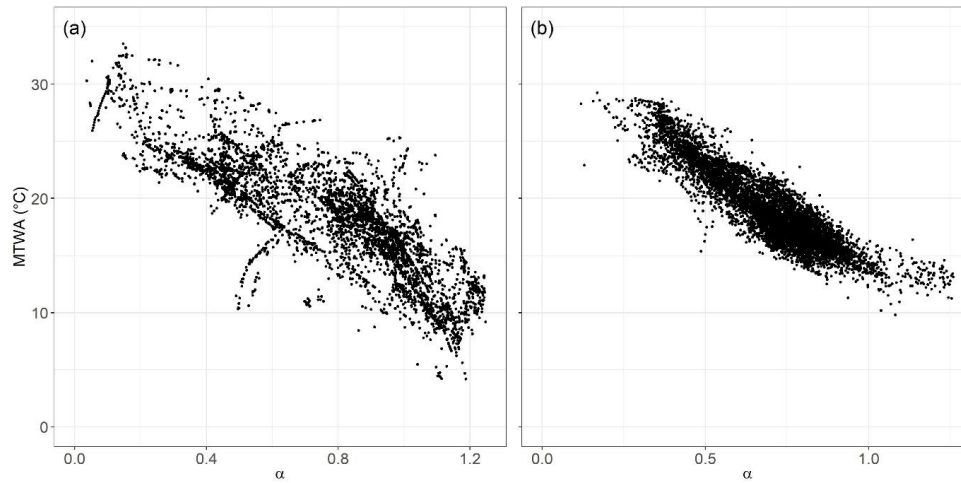
549



550 Figure 4. Changes in the west-east gradient of plant-available moisture as represented by  
551 anomalies in  $\alpha$  relative to 0.5 ka at individual sites through the Holocene. The red lines show  
552 the regression lines. The shades indicate the 95 % confidence intervals of the regression lines.  
553



555 Figure 5. The relationship between mean temperature of the warmest month (MTWA) and  
556 plant-available moisture as represented by  $\alpha$  (a) in the modern climate data set, and (b) in the  
557 Holocene reconstructions.  
558



559

560 Table 1. Leave-out cross-validation (with geographically and climatically close sites  
 561 removed) fitness of the modified version of fxTWA-PLS, for mean temperature of the coldest  
 562 month (MTCO), mean temperature of the warmest month (MTWA) and plant-available  
 563 moisture ( $\alpha$ ), with p-spline smoothed fx estimation, using bins of 0.02, 0.02 and 0.002,  
 564 showing results for all the components. RMSEP is the root-mean-square error of prediction.  
 565  $\Delta$ RMSEP is the per cent change of RMSEP using the current number of components than  
 566 using one component less.  $p$  assesses whether using the current number of components is  
 567 significantly different from using one component less, which is used to choose the last  
 568 significant number of components (indicated in bold) to avoid over-fitting. The degree of  
 569 overall compression is assessed by linear regression of the cross-validated reconstructions  
 570 onto the climate variable,  $b_1$ ,  $b_{1.se}$  are the slope and the standard error of the slope,  
 571 respectively. The closer the slope ( $b_1$ ) is to 1, the less the overall compression is.  
 572  
 573

	ncomp	$R^2$	avg. bias	max. bias	min. bias	RMSEP	$\Delta$ RMSEP	$p$	$b_1$	$b_{1.se}$
MTCO	1	0.70	-0.86	25.23	0.00	5.20	-39.97	0.001	0.89	0.01
	2	0.73	-0.73	25.00	0.00	4.87	-6.29	0.001	0.91	0.01
	3	0.74	-0.71	24.38	0.00	4.86	-0.32	0.001	0.91	0.01
	<b>4</b>	<b>0.75</b>	<b>-0.59</b>	<b>24.27</b>	<b>0.00</b>	<b>4.70</b>	<b>-3.26</b>	<b>0.001</b>	<b>0.91</b>	<b>0.01</b>
	5	0.74	-0.63	34.54	0.00	4.77	1.51	1.000	0.91	0.01
MTWA	1	0.52	-0.29	17.13	0.00	3.72	-26.88	0.001	0.69	0.01
	2	0.56	-0.14	17.20	0.00	3.53	-5.06	0.001	0.71	0.01
	3	0.56	-0.13	17.01	0.00	3.53	-0.20	0.008	0.71	0.01
	<b>4</b>	<b>0.57</b>	<b>-0.11</b>	<b>17.30</b>	<b>0.00</b>	<b>3.47</b>	<b>-1.56</b>	<b>0.001</b>	<b>0.71</b>	<b>0.01</b>
	5	0.57	-0.11	17.34	0.00	3.48	0.10	0.780	0.71	0.01
$\alpha$	1	0.65	-0.014	0.787	0.000	0.165	-39.59	0.001	0.76	0.01
	2	0.68	-0.016	0.781	0.000	0.159	-3.55	0.001	0.77	0.01
	<b>3</b>	<b>0.68</b>	<b>-0.017</b>	<b>0.757</b>	<b>0.000</b>	<b>0.158</b>	<b>-0.61</b>	<b>0.023</b>	<b>0.78</b>	<b>0.01</b>
	4	0.69	-0.017	0.784	0.000	0.158	-0.43	0.108	0.79	0.01
	5	0.69	-0.017	0.850	0.000	0.158	0.26	0.985	0.80	0.01

574





575 Table 2. Canonical Correspondence Analysis (CCA) result of modern and fossil-  
 576 reconstructed MTCO, MTWA and  $\alpha$ . The summary statistics for the ANOVA-like  
 577 permutation test (999 permutations) are also shown. VIF is the variance inflation factor, Df is  
 578 the number of degrees of freedom,  $\chi^2$  is the constrained eigenvalue (or the sum of  
 579 constrained eigenvalues for the whole model), F is significance, and Pr (>F) is the  
 580 probability.  
 581

	<b>Axes</b>	<b>Axis 1</b>	<b>Axis 2</b>	<b>Axis 3</b>	<b>VIF</b>
		Constrained eigenvalues	0.3819	0.1623	0.1087
Modern	<b>Correlations of the environmental variables with the axes:</b>				
	MTCO	-0.815	0.579	0.012	1.31
	MTWA	-0.700	-0.203	0.685	3.34
	$\alpha$	0.883	0.430	-0.187	3.39
		<b>Df</b>	<b><math>\chi^2</math></b>	<b>F</b>	<b>Pr (&gt;F)</b>
	Whole model	3	0.6530	78.113	0.001
	MTCO	1	0.3082	110.597	0.001
	MTWA	1	0.1602	57.489	0.001
	$\alpha$	1	0.1846	66.252	0.001
	CCA 1	1	0.3819	137.076	0.001
	CCA 2	1	0.1623	58.252	0.001
	CCA 3	1	0.1087	39.011	0.001
	Fossil-reconstructed	<b>Axes</b>	<b>Axis 1</b>	<b>Axis 2</b>	<b>Axis 3</b>
Constrained eigenvalues		0.3594	0.2270	0.2043	/
<b>Correlations of the environmental variables with the axes:</b>					
MTCO		0.417	0.767	0.488	1.33
MTWA		0.987	0.146	-0.068	5.31
$\alpha$		-0.945	0.095	-0.311	5.19
		<b>Df</b>	<b><math>\chi^2</math></b>	<b>F</b>	<b>Pr (&gt;F)</b>
Whole model		3	0.7906	225.12	0.001
MTCO		1	0.2446	208.91	0.001
MTWA		1	0.3309	282.65	0.001
$\alpha$		1	0.2152	183.79	0.001
CCA 1		1	0.3594	307.00	0.001
CCA 2		1	0.2270	193.88	0.001
CCA 3	1	0.2043	174.48	0.001	



583 Table 3. Assessment of the significance of anomalies to 0.5 ka through time with latitude and  
 584 elevation. The slope is obtained by linear regression of the anomaly onto the longitude or  
 585 elevation.  $p$  is the significance of the slope (bold parts:  $p < 0.05$ ).  $x_0$  is the point where the  
 586 anomaly is 0 in the linear equation, which indicates longitude or elevation where the anomaly  
 587 changes sign.  
 588

	age (ka)	Longitude (°E)			Elevation (km)		
		slope	$p$	$x_0$	slope	$p$	$x_0$
MTCO (°C)	0.5	0.00	/	/	0.00	/	/
	1.5	-0.07	0.453	-13.80	-0.39	0.285	-0.71
	2.5	-0.14	0.113	-8.52	-0.52	0.170	-0.29
	3.5	-0.14	0.253	-13.06	-0.79	0.147	-0.72
	4.5	-0.12	0.445	-16.97	-0.69	0.315	-1.37
	5.5	-0.24	0.260	-9.37	-0.63	0.477	-1.17
	6.5	-0.17	0.405	-12.79	-0.88	0.281	-0.71
	7.5	-0.16	0.391	-18.89	-1.43	0.067	-0.55
	8.5	-0.08	0.703	-33.59	-1.34	0.101	-0.42
	9.5	0.00	0.992	937.82	-1.81	0.056	0.14
	10.5	0.19	0.493	9.85	-1.38	0.232	-0.62
	11.5	0.23	0.528	13.77	0.12	0.947	36.35
MTWA (°C)	0.5	0.00	/	/	0.00	/	/
	1.5	0.00	0.928	-51.95	-0.04	0.859	-4.94
	2.5	-0.09	0.164	-2.90	-0.48	0.069	1.15
	3.5	<b>-0.22</b>	<b>0.007</b>	-1.84	-0.44	0.236	1.76
	4.5	<b>-0.22</b>	<b>0.014</b>	-2.08	-0.57	0.140	1.56
	5.5	<b>-0.29</b>	<b>0.005</b>	-2.62	-0.43	0.340	1.49
	6.5	<b>-0.24</b>	<b>0.015</b>	-2.28	-0.61	0.134	1.43
	7.5	<b>-0.27</b>	<b>0.010</b>	-3.05	<b>-1.03</b>	<b>0.021</b>	1.28
	8.5	<b>-0.26</b>	<b>0.024</b>	-2.62	-0.87	0.079	1.51
	9.5	<b>-0.32</b>	<b>0.012</b>	-3.17	-0.44	0.457	1.36
	10.5	-0.18	0.110	-1.21	0.54	0.278	0.42
	11.5	0.13	0.453	-7.25	0.37	0.663	0.22
$\alpha$	0.5	0.00	/	/	0.00	/	/
	1.5	0.00	0.453	7.55	-0.01	0.438	3.67
	2.5	0.00	0.526	-10.41	0.02	0.211	0.21
	3.5	<b>0.01</b>	<b>0.006</b>	-4.78	0.02	0.161	0.38
	4.5	<b>0.01</b>	<b>0.009</b>	-4.60	<b>0.05</b>	<b>0.008</b>	0.79
	5.5	<b>0.01</b>	<b>0.003</b>	-4.73	<b>0.05</b>	<b>0.031</b>	0.65
	6.5	<b>0.01</b>	<b>0.007</b>	-5.28	<b>0.06</b>	<b>0.003</b>	0.64
	7.5	<b>0.02</b>	<b>0.008</b>	-5.99	<b>0.09</b>	<b>0.000</b>	0.75
	8.5	<b>0.02</b>	<b>0.018</b>	-6.45	<b>0.08</b>	<b>0.004</b>	0.68
	9.5	<b>0.01</b>	<b>0.046</b>	-6.29	<b>0.07</b>	<b>0.012</b>	0.72
	10.5	0.01	0.173	-4.70	0.02	0.523	0.67
	11.5	0.00	0.713	-2.76	0.03	0.654	0.93

590 **Appendix A**

591 **Theoretical basis:**

592 **The previous version of fxTWA-PLS (fxTWA-PLS1):**

593 The estimated optimum ( $\hat{u}_k$ ) and unbiased tolerance ( $\hat{t}_k$ ) of each taxon are calculated from  
 594 the modern training data set as follows:

$$595 \hat{u}_k = \frac{\sum_{i=1}^n y_{ik} x_i}{\sum_{i=1}^n y_{ik}} \quad (A1)$$

$$596 \hat{t}_k = \sqrt{\frac{\sum_{i=1}^n y_{ik} (x_i - \hat{u}_k)^2}{(1 - 1/N_{2k}) \sum_{i=1}^n y_{ik}}} \quad (A2)$$

597 where

$$598 N_{2k} = \frac{1}{\sum_{i=1}^n \left( \frac{y_{ik}}{\sum_{i'=1}^n y_{i'k}} \right)^2} \quad (A3)$$

599 where  $n$  is the total number of sites;  $y_{ik}$  is the observed abundance of the  $k^{th}$  taxon at the  $i^{th}$   
 600 site;  $x_i$  is the observed climate value at the  $i^{th}$  site;  $N_{2k}$  is the effective number of occurrences  
 601 for the  $k^{th}$  taxon.

602 fx correction is applied as weight in the form of  $1/fx^2$  at regression at step 7 in Table 1 in Liu  
 603 et al. (2020). The regression step uses robust linear model fitting by the R code:

$$604 \quad rlm(x_i \sim comp_1 + comp_2 + \dots + comp_{pls}, weights = 1/fx^2) \quad (A4)$$

607 **The modified version of fxTWA-PLS (fxTWA-PLS2):**

608 The distribution of  $y_{ik}$  is influenced by the distribution of the climate variable, so we need to  
 609 apply the fx correction when calculating optimum and tolerance for each taxon as follows:

$$610 \hat{u}_k = \frac{\sum_{i=1}^n \frac{y_{ik} x_i}{f_{x_i}}}{\sum_{i=1}^n \frac{y_{ik}}{f_{x_i}}} \quad (A5)$$

$$611 \hat{t}_k = \sqrt{\frac{\sum_{i=1}^n \frac{y_{ik} (x_i - \hat{u}_k)^2}{f_{x_i}}}{\left(1 - \frac{1}{N_{2k}}\right) \sum_{i=1}^n \frac{y_{ik}}{f_{x_i}}}} \quad (A6)$$

612 where

$$613 N_{2k} = \frac{1}{\sum_{i=1}^n \left( \frac{\frac{y_{ik}}{f_{x_i}}}{\sum_{i'=1}^n \frac{y_{i'k}}{f_{x_{i'}}}} \right)^2} \quad (A7)$$

614 The modified version of fxTWA-PLS applies fx correction separately at taxon calculation  
 615 and regression (step 2 and 7 in Table 1 in Liu et al., 2020), both using weight in the form of  
 616  $1/fx$ . The regression step (step 7) then becomes:



617 
$$rlm(x_i \sim comp_1 + comp_2 + \dots + comp_{pls}, weights = 1/f_x) \quad (A8)$$

618 The previous version uses  $f_x$  values extracted from histograms, and different bin widths may  
619 result in different training results. The modified version applies P-splines histogram  
620 smoothing (Eilers and Marx, 2021) with third order difference penalty, which makes the  $f_x$   
621 values almost independent on the bin width. The optimal smoothing parameter of the P-spline  
622 penalty was determined by the HFS (Harville-Fellner-Schall) algorithm (Eilers and Marx,  
623 2021) for the Poisson likelihood for the histogram counts.

624 Table A1. Leave-out cross-validation (with geographically and climatically close sites removed)  
 625 fitness of the previous and modified version of fxTWA-PLS (fxTWA-PLS1 and fxTWA-PLS2,  
 626 respectively), for mean temperature of the coldest month (MTCO), mean temperature of the warmest  
 627 month (MTWA) and plant-available moisture ( $\alpha$ ), using bins of 0.02, 0.02 and 0.002, respectively.  $n$   
 628 is the number of components used. RMSEP is the root mean square error of prediction.  $\Delta$ RMSEP is  
 629 the per cent change of RMSEP using the current number of components than using one component  
 630 less.  $p$  assesses whether using the current number of components is significantly different from using  
 631 one component less, which is used to choose the last significant number of components (indicated in  
 632 bold) to avoid overfitting. The degree of overall compression is assessed by doing linear regression to  
 633 the cross-validation result and the climate variable.  $b1$ ,  $b1.se$  are the slope and the standard error of  
 634 the slope, respectively. The closer the slope ( $b1$ ) is to 1, the lower the overall compression is.  $fx$   
 635 correction is set intrinsic in functions in  $fxTWA_{PLS}$  package for both versions in this paper, instead  
 636 of relying on an outside input in Liu et al. (2020), so the values of fxTWA-PLS1 might be slighted  
 637 different from values in Table 2 in Liu et al. (2020), but it doesn't affect the conclusion.  
 638

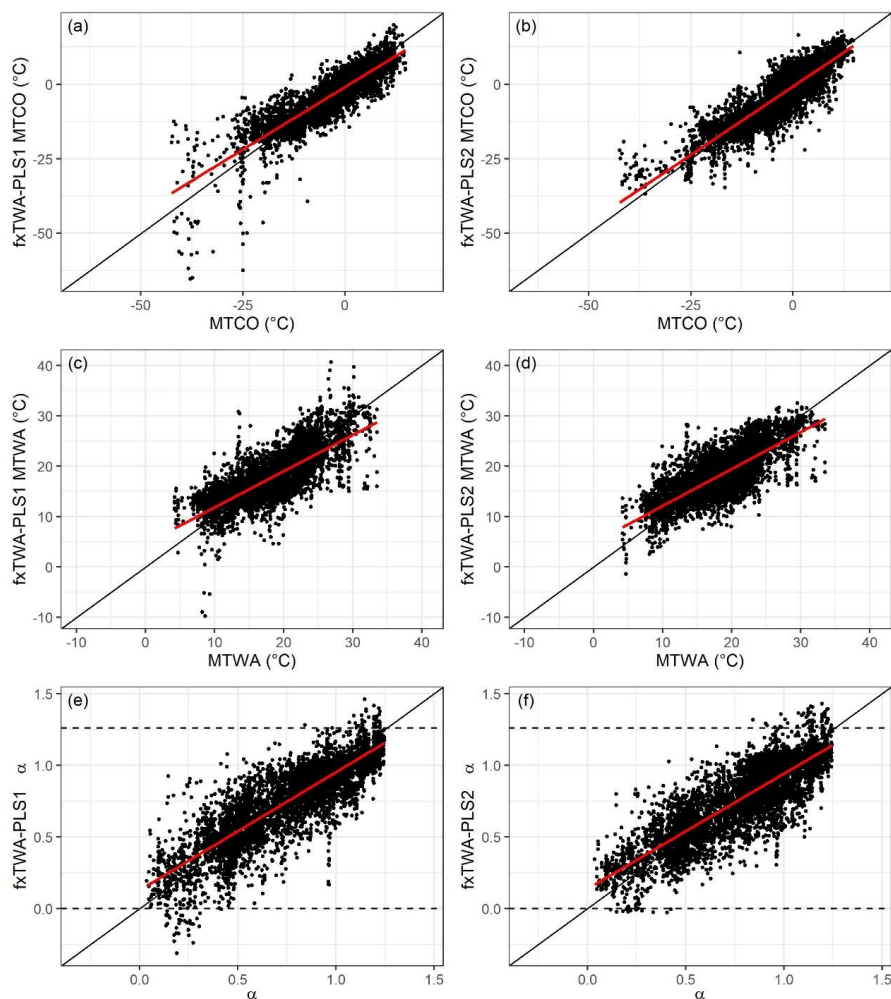
	Method	$n$	$R^2$	avg. bias	max. bias	min. bias	RMSEP	$\Delta$ RMSEP	$p$	$b1$	$b1.se$
MTCO	fxTWA-PLS1	1	0.66	-0.86	31.17	0.00	5.21	-39.87	0.001	0.76	0.01
		2	0.72	-0.52	36.65	0.00	4.70	-9.78	0.001	0.80	0.01
		3	0.73	-0.47	41.18	0.00	4.62	-1.63	0.001	0.82	0.01
		<b>4</b>	<b>0.73</b>	<b>-0.51</b>	<b>44.86</b>	<b>0.00</b>	<b>4.58</b>	<b>-1.01</b>	<b>0.006</b>	<b>0.82</b>	<b>0.01</b>
		5	0.73	-0.41	58.35	0.00	4.62	0.89	0.708	0.83	0.01
	fxTWA-PLS2	1	0.70	-0.86	25.23	0.00	5.20	-39.97	0.001	0.89	0.01
		2	0.73	-0.73	25.00	0.00	4.87	-6.29	0.001	0.91	0.01
		3	0.74	-0.71	24.38	0.00	4.86	-0.32	0.001	0.91	0.01
		<b>4</b>	<b>0.75</b>	<b>-0.59</b>	<b>24.27</b>	<b>0.00</b>	<b>4.70</b>	<b>-3.26</b>	<b>0.001</b>	<b>0.91</b>	<b>0.01</b>
		5	0.74	-0.63	34.54	0.00	4.77	1.51	1.000	0.91	0.01
	fxTWA-PLS1	1	0.50	-0.53	17.91	0.00	3.87	-24.09	0.001	0.67	0.01
		<b>2</b>	<b>0.56</b>	<b>-0.54</b>	<b>17.71</b>	<b>0.00</b>	<b>3.52</b>	<b>-8.98</b>	<b>0.001</b>	<b>0.69</b>	<b>0.01</b>
		3	0.57	-0.49	25.14	0.00	3.52	0.09	0.565	0.73	0.01
		4	0.57	-0.43	34.92	0.00	3.56	1.12	0.974	0.75	0.01
		5	0.57	-0.46	32.23	0.00	3.55	-0.23	0.139	0.74	0.01
fxTWA-PLS2	1	0.52	-0.29	17.13	0.00	3.72	-26.88	0.001	0.69	0.01	
	2	0.56	-0.14	17.20	0.00	3.53	-5.06	0.001	0.71	0.01	
	3	0.56	-0.13	17.01	0.00	3.53	-0.20	0.008	0.71	0.01	
	<b>4</b>	<b>0.57</b>	<b>-0.11</b>	<b>17.30</b>	<b>0.00</b>	<b>3.47</b>	<b>-1.56</b>	<b>0.001</b>	<b>0.71</b>	<b>0.01</b>	
	5	0.57	-0.11	17.34	0.00	3.48	0.10	0.780	0.71	0.01	
$\alpha$	fxTWA-PLS1	1	0.63	-0.020	0.773	0.000	0.174	-36.23	0.001	0.78	0.01
		2	0.69	-0.012	0.902	0.000	0.157	-9.66	0.001	0.79	0.01
		<b>3</b>	<b>0.69</b>	<b>-0.011</b>	<b>0.820</b>	<b>0.000</b>	<b>0.155</b>	<b>-1.28</b>	<b>0.001</b>	<b>0.79</b>	<b>0.01</b>
		4	0.70	-0.010	0.786	0.000	0.156	0.25	0.867	0.81	0.01
		5	0.70	-0.010	0.786	0.000	0.156	0.09	1.000	0.81	0.01
	fxTWA-PLS2	1	0.65	-0.014	0.787	0.000	0.165	-39.59	0.001	0.76	0.01
		2	0.68	-0.016	0.781	0.000	0.159	-3.55	0.001	0.77	0.01
		<b>3</b>	<b>0.68</b>	<b>-0.017</b>	<b>0.757</b>	<b>0.000</b>	<b>0.158</b>	<b>-0.61</b>	<b>0.023</b>	<b>0.78</b>	<b>0.01</b>
		4	0.69	-0.017	0.784	0.000	0.158	-0.43	0.108	0.79	0.01
		5	0.69	-0.017	0.850	0.000	0.158	0.26	0.985	0.80	0.01

639

640

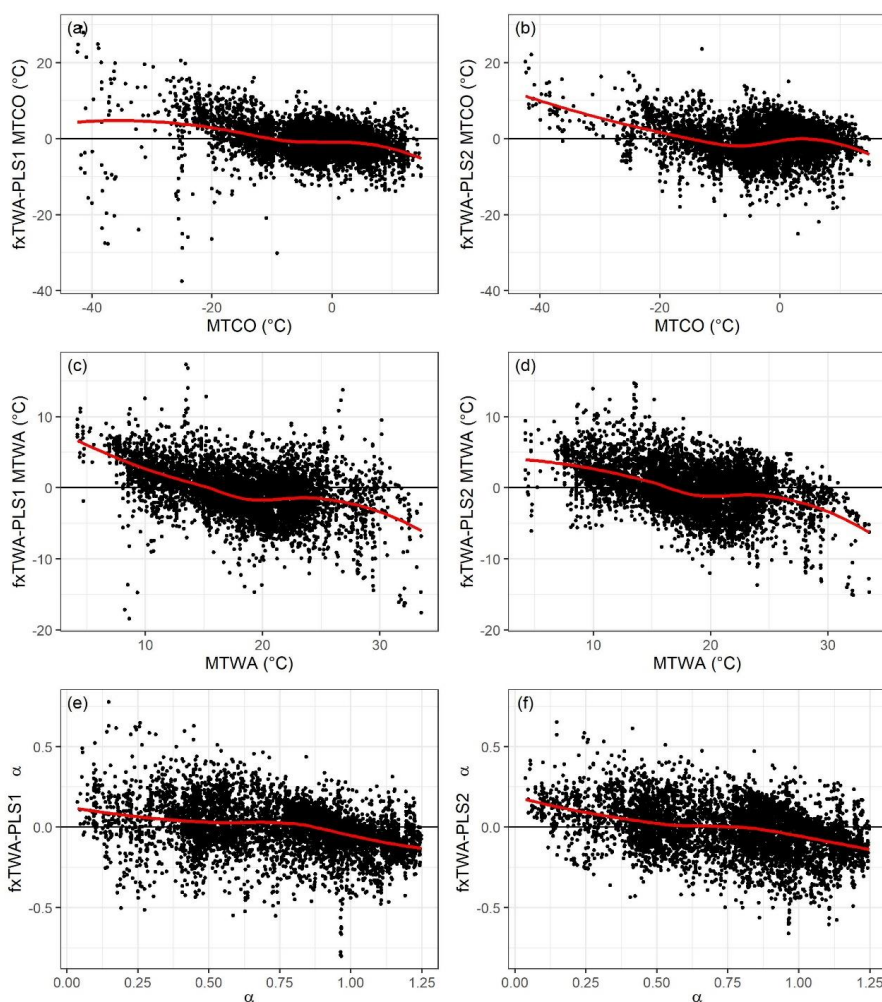


641 Figure A1. Training results using the last significant number of components. The left panel  
642 shows the previous version (fxTWA-PLS1) and the right panel shows the modified version of  
643 fxTWA-PLS (fxTWA-PLS2). The 1: 1 line is shown in black; the linear regression line is  
644 shown in red, to show the degree of overall compression. The horizontal dashed lines indicate  
645 the natural limit of  $\alpha$  (0~1.26).  
646



647  
648

649 Figure A2. Residuals using the last significant number of components. The left panel shows  
650 the previous version (fxTWA-PLS1) and the right panel shows the modified version (fxTWA-  
651 PLS2) of fxTWA-PLS. The zero line is shown in black; the locally estimated scatterplot  
652 smoothing is shown in red, to show the degree of local compression.  
653



654

655 As shown in Table A1, Figure A1 and A2, the modified version is able to further reduce the  
656 compression in MTCO and MTWA, and maximum bias in MTCO, MTWA and  $\alpha$ . As shown  
657 in Figure A1 and A2, there is less scatter and there are less  $\alpha$  values beyond the natural limit.